J. Fluid Mech. (2009), *vol.* 622, *pp.* 75–102.
doi:10.1017/S0022112008005077 Printed in the United Kingdom

Unsteady natural convection in a triangular enclosure induced by absorption of radiation – a revisit by improved scaling analysis

YADAN MAO†, CHENGWANG LEI AND JOHN C. PATTERSON

School of Engineering, James Cook University, Townsville, QLD 4811, Australia

(Received 14 April 2008 and in revised form 11 September 2008)

The present study is concerned with radiation-induced natural convection in a water-filled triangular enclosure with a sloping bottom, which is directly relevant to buoyancy-driven flows in littoral regions. An improved scaling analysis is carried out to reveal more detailed features of the flow than a previously reported analysis. Two critical functions of the Rayleigh number with respect to the horizontal position are derived from the scaling for identifying the distinctness and stability of the thermal boundary layer. Four flow scenarios are possible, depending on the bottom slope and the maximum water depth. For each flow scenario, the flow domain may be composed of multiple subregions with distinct thermal and flow features, depending on the Rayleigh number. The dividing points between neighbouring subregions are determined by comparisons of the critical functions of the Rayleigh number with the global Rayleigh number. Position-dependent scales have been established to quantify the flow properties in different subregions. The different flow regimes for the case with relatively large bottom slopes and shallow waters are examined in detail. The present scaling results are verified by numerical simulations.

1. Introduction

Investigations of geophysical natural convection began with shallow rectangular cavities with thermal forcing applied on vertical endwalls, for which a large body of literature exists (e.g. Hart 1972; Cormack, Leal & Imberger 1974*a*, *b*; Imberger 1974; Bejan & Rossie 1981; Bejan, Al-Homoud & Imberger 1981). Physical scaling analysis (Patterson & Imberger 1980; Patterson 1984) has provided important insight into the transient development of the buoyancy-driven flow under this configuration. Subsequently, spatial variations of the radiation absorption property have been considered in order to provide a closer representation of the real situation (e.g. Trevisan & Bejan 1986; Coates & Patterson 1993, 1994). In these cases, a cavity-wide flow is formed to adjust the horizontal temperature gradient in response to the unequal absorption of radiation.

However, the rectangular model described above is not adequate for representing the near-shore geometry. The bathymetry variation across the shore in the littoral region implies that a triangular geometry is a better representation. In fact, it is this geometry that captures an important mechanism for the generation of fluid

† Email address for correspondence: yadan.mao@jcu.edu.au

motion. Since the approximately equal heat flux entering or leaving through the water surface is distributed over different depths of water, the water at any given location becomes either hotter or cooler than its horizontal neighbouring region, and thus a horizontal temperature gradient is established. As a consequence, the temperature-induced horizontal density gradient then promotes exchange between littoral and open waters.

Field observations (Adams & Wells 1984; Monismith, Imberger & Morison 1990) have demonstrated the significance of this buoyancy-induced horizontal exchange flow due to bathymetry variation of the near-shore water, which is sometimes referred to as a 'thermal siphon'. The functioning of the thermal siphon substantially reduces the time required to replace the water in the sidearm. A recent field experiment by Monismith *et al.* (2006) indicates that the thermal siphon may be a generic feature of the hydrodynamics of coral reefs and coastal oceans in general.

While the thermal forcing in field situations varies over the diurnal cycle, this paper, as well as Farrow & Patterson (1993*b*, 1994) and Lei & Patterson (2002, 2003) addresses the simplest forcing case: that of a suddenly applied constant radiative heating. An understanding of this case will provide insight into the more complex case of unsteady, including diurnal, forcing. During the daytime, the water body absorbs solar radiation in an exponentially decaying manner with depth according to Beers' law. Typically, in natural water bodies, most radiation is absorbed within a depth of about 1–2 m from the water surface, resulting in a shallow surface layer with water much warmer than the underlying water. The depth of this surface layer is termed the penetration depth of solar radiation, which depends on the spectral distribution of the radiation and the turbidity of the water. For the near-shore region with water depth less than the penetration depth, two theoretical models have been proposed to explain the occurrence of an increasing temperature towards the shore which drives a surface outflow from the edge of the sidearm. One model assumes that all of the radiation is absorbed and uniformly distributed over the local water depth (Farrow & Patterson 1993*a*; Farrow 2004; Monismith *et al.* 2006), resulting in the water temperature being inversely proportional to the water depth. The other model (Farrow & Patterson 1994; Lei & Patterson 2002) is more physically realistic: it takes into account the exponentially decaying absorption of solar radiation, and assumes that any residual radiation arriving at the bottom slope is absorbed by the bottom, and re-emitted as a bottom heat flux, which is a potential source for Rayleigh–Bénard instability. Therefore, the bottom heat flux increases shorewards, resulting in a temperature gradient that drives the flow up the slope in the bottom boundary layer and outwards in the surface layer.

Based on a small-slope assumption, the zero-order asymptotic solution of Farrow & Patterson (1994) quantifies the circulation induced by absorption of radiation in a sidearm. The solution has shed light on the temporal and spatial variations of the thermal flow. However, the nature of the zero-order asymptotic solution of Farrow & Patterson (1994) implies that the effects of convection or horizontal conduction, which are both second-order effects, were excluded. These effects were included in the recent asymptotic solution of Farrow (2004) for periodically forced natural convection over a slowly varying topography. As mentioned above, the theoretical model of Farrow (2004) assumes that the radiation energy and heat loss is uniformly distributed over the local water depth.

In the stability analysis of Farrow & Patterson (1993*b*), which was based on the above-mentioned zero-order asymptotic solution and assumed that longitudinal vortices were the form of instability, the local critical Grashof number for the onset

of instability at different horizontal positions was obtained both analytically and numerically. Although some divergence exists between the two solutions at large horizontal positions, both the analytical and numerical solutions reveal that, under sufficiently high Grashof numbers, instability caused by the bottom heat flux would occur only in a region centred away from the shore.

Efforts to understand natural convection in the sidearm have also been made through scaling analysis. Lei & Patterson (2002) focused on shallow waters with water depth less than the penetration depth of radiation. The scaling classified the overall flow state at different Rayleigh numbers into three distinct flow regimes: conductive; transitional; and convective. However, the scaling analysis did not capture the distinctive flow regions and the variation of thermal flow properties with offshore distance, which have been reported in the numerical simulation of Mao, Lei & Patterson (2007).

Identifying the different flow regions through scaling will provide an important insight into the detailed exchange and mixing processes, as the transportation processes vary significantly in different regions of the sidearm. For instance, owing to the occurrence of rising thermal plumes in the unstable region, vertical transport there is much stronger than in the stable region. Moreover, quantifying the variation of flow velocity with offshore distance would be desirable for assessing the contribution of radiation-induced natural convection to horizontal exchanges at various offshore distances.

A survey of the literature indicates that no existing physical scaling has captured the above-mentioned spatial variation of the thermal flow in a triangular domain subject to radiative heating. This has motivated the present investigation which will reveal detailed scenarios of the thermal flow at different parametric settings and the variation of the flow features with offshore distance. In the following sections, an extended scaling analysis is developed and later verified by numerical simulations. The major advancement of the present scaling compared with the scaling by Lei & Patterson (2002) is that horizontal dependency is retained throughout the scaling process. As a consequence, detailed features of the flow at different offshore distances are revealed, and a more complete scenario of the flow at different parametric settings is illustrated.

With the potential geophysical applications in mind, the region near the tip of the triangular enclosure is termed the near-shore region and the region far from the tip is termed the offshore region. In the field situation under conditions of high radiation input, the flow may become turbulent. The present scaling analysis is limited to laminar conditions with a constant molecular viscosity, approaching the transition to turbulence when instabilities occur. Turbulence models are outside the scope of this paper.

2. Model formulation

In near-shore regions of geophysical water bodies, topography variations alongshore are often less significant than across shore, and thus a two-dimensional wedge is an appropriate geometric model to characterize the depth variation in these regions. The model under consideration is sketched in figure 1, which has a bottom slope of A and a depth of h with the water surface represented by the horizontal side. Although a much more complex bathymetry may exist in field situations, the present model aims to capture the basic flow mechanisms induced by the depth variation across the shore, and thus the simple wedge model is sufficient. Further, a two-dimensional flow

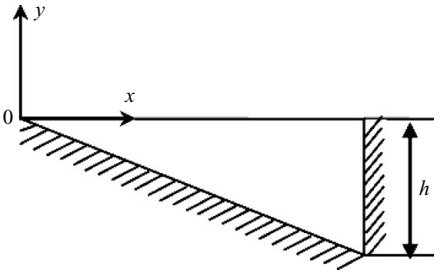

FIGURE 1. Geometry of the flow domain.

is assumed in this investigation despite the potential for the flow to become three-dimensional when instabilities occur. The adoption of a two-dimensional numerical model for this type of flow has been justified in Lei & Patterson (2005). With the Boussinesq assumption, the two-dimensional Navier–Stokes and energy equations governing the flow and temperature evolution within the wedge are:

$$\frac{\partial u}{\partial x} + \frac{\partial v}{\partial y} = 0, \tag{1}$$

$$\frac{\partial u}{\partial t} + u\frac{\partial u}{\partial x} + v\frac{\partial u}{\partial y} = -\frac{1}{\rho_0}\frac{\partial p}{\partial x} + \nabla^2 u, \tag{2}$$

$$\frac{\partial v}{\partial t} + u\frac{\partial v}{\partial x} + v\frac{\partial v}{\partial y} = -\frac{1}{\rho_0}\frac{\partial p}{\partial y} + \nu\nabla^2 v + g\beta(T - T_0), \tag{3}$$

$$\frac{\partial T}{\partial t} + u\frac{\partial T}{\partial x} + v\frac{\partial T}{\partial y} = k\nabla^2 T + S(x, y, t), \tag{4}$$

where u and v are the velocity components in the horizontal and vertical direction, respectively; x and y are the horizontal and vertical coordinates originating from the tip; T is the fluid temperature; and P is the pressure. The density, kinematic viscosity, thermal diffusivity and thermal expansion coefficient of the fluid at the reference temperature T_0 are ρ_0, ν, k and β, respectively. $S(x, y, t)$ in (4) represents the internal heating source due to absorption of solar radiation, which is given by (refer to Farrow & Patterson 1994; Lei & Patterson 2002):

$$S = \frac{I_0}{\rho_0 C_p}\eta e^{\eta y} = H_0\eta e^{\eta y} (y \leqslant 0), \tag{5}$$

where I_0 represents the radiation intensity at the water surface, C_P is the specific heat of water at the reference temperature, and η is the attenuation coefficient (Rabl & Nielsen 1975). Here, for simplification, η is considered constant throughout the whole water body.

In the present model, the initial condition of the flow is stationary and isothermal. Rigid non-slip velocity boundary conditions ($u = v = 0$) are assumed for the endwall and the bottom slope, whereas the water surface is stress free ($\partial u/\partial y = 0$ and $v = 0$). An adiabatic temperature condition is assumed at the water surface and the endwall. On the bottom slope, the heat flux resulting from the re-emission of the residual radiation arriving at the bottom is

$$\frac{\partial T}{\partial \hat{n}} = -\frac{1}{k}H_0 e^{-A\eta x}, \tag{6}$$

where $\hat{n}$ is the direction normal to the sloping bottom. It is clear from the above equation that the bottom heat flux varies with the horizontal location.

It is worth noting that the following scaling analysis is conducted for an unbounded wedge domain, and thus the endwall has no relevance to the scaling. However, the endwall is assumed for the numerical simulations so that calculations can be carried out in a finite domain. The effect of an endwall on the simulation results of thermal flow induced by the diurnal thermal cycle is discussed in detail in Farrow (2004). For the present model, the presence of the endwall in the simulation, forces the flow to change its course at the deep end, resulting in a region near the endwall which is affected by the return flow. Therefore, for the later verification of the scaling using simulation results, flow properties from the simulation were selected from positions sufficiently far from the endwall to avoid the endwall effect.

3. Scaling analysis

3.1. *Initial stage of boundary-layer development*

The water body in the shallow region is heated through two independent mechanisms: first, the direct absorption of radiation by the water body, represented by the source term $S(x, y, t)$ in the energy equation, which decays with the water depth, resulting in a stable stratification; and secondly, the heat flux emitted by the bottom surface (equation (6)). Both the source term and the bottom heat flux are time independent. The stable stratification induced by the former mechanism implies that no flow is generated through this mechanism. On the other hand, a thermal boundary layer adjacent to the sloping bottom is generated by the latter mechanism, and within this boundary layer, a horizontal temperature gradient generates a thermal flow up the bottom slope. Furthermore, the adverse vertical temperature gradient near the bottom is a potential source for thermal instability.

Within the thermal boundary layer, the water temperature increases owing to both the heat flux from the bottom surface and the direct absorption of radiation. A balance between the unsteady term and the source term in the energy equation yields a temperature growth scale due to the absorption of radiation:

$$T_a \sim H_0 \eta \, \mathrm{e}^{\eta y} t. \tag{7}$$

A balance between the unsteady term and the diffusion term yields a scale for the thickness of the thermal boundary layer

$$\delta_T \sim (kt)^{1/2}. \tag{8}$$

According to (6), the temperature increase within the thermal boundary layer due to the bottom heat flux can be expressed as

$$T_b \sim \frac{1}{k} H_0 \delta_T \mathrm{e}^{-A\eta x} \sim k^{-1/2} t^{1/2} H_0 \mathrm{e}^{-A\eta x}. \tag{9}$$

The above scale shows that the temperature in the thermal boundary layer increases with time, but decreases exponentially with the horizontal position x.

The exponential terms in both (7) and (9) were approximated to be $O(1)$ in Lei & Patterson (2002) under a shallow-water assumption of $h < \eta^{-1}$. However, these exponential terms are retained in the present study in order to reveal the position-dependent flow features.

To evaluate the relative importance of the source term and the bottom heat flux in raising the water temperature in the bottom boundary layer, the temperature scale (7)

is compared with the scale (9), which yields that, when $t < (k\eta^2)^{-1}$, the bottom heat flux dominates the temperature growth in the thermal boundary layer. It will be shown later that $(k\eta^2)^{-1}$ is a very large time scale compared to other time scales of the flow development. Hence, in the following scaling, the bottom heat flux is considered to be the dominant thermal forcing.

As soon as the radiation is initiated, the thermal boundary layer starts to grow. The horizontal temperature gradient within the thermal boundary layer induces a buoyancy term in the momentum equation that drives a flow up the bottom slope. In most field situations, the slope of near-shore waters is very small, indicating that the thermal boundary layer above the sloping bottom is approximately horizontal, and thus the thickness of the thermal boundary layer represents its vertical length scale, and the vertical component of the flow velocity is negligible compared to the horizontal component. In the vertical momentum equation, a balance between the buoyancy term and the pressure term yields a scale for the pressure difference within the thermal boundary layer:

$$P \sim g\beta\rho_0 T_b \delta_T \sim g\beta\rho_0 H_0 \mathrm{e}^{-A\eta x} t. \tag{10}$$

This pressure difference acts along the thermal boundary layer and drives a flow up the slope with a velocity governed by the horizontal momentum transfer. In the horizontal momentum equation, a comparison among the unsteady inertia term $O(u/t)$, the advection term $O(u^2/x)$ and the viscous term $O(\nu u/\delta_T^2)$ shows that the viscous term dominates among the three terms for $Pr > 1$ and $ut/x < Pr$, where Pr is the Prandtl number defined as

$$Pr = \nu/k. \tag{11}$$

Therefore, for a fluid with $Pr > 1$ (such as water considered here), at the early stage when $ut < Prx$, the balance of the horizontal momentum transfer is between the pressure gradient and the viscous term, which yields a velocity scale

$$u \sim g\beta H_0 \mathrm{e}^{-A\eta x} \frac{kt^2}{\nu x} \sim Ra \frac{t^2 k^3}{h^4 x} \mathrm{e}^{-A\eta x}, \tag{12}$$

where Ra is the Rayleigh number defined as

$$Ra = \frac{g\beta H_0 h^4}{\nu k^2}. \tag{13}$$

It is worth noting that in the scaling of Lei & Patterson (2002), the horizontal length scale was taken as the full length of the thermal boundary layer $L = h/A$. However, a fixed length scale in the scaling obscures the horizontal dependency of the flow, which will be revealed below by adopting a variable horizontal length scale x.

3.2. *Steady state of the boundary layer*

In the thermal boundary layer, the heat conducted into the boundary layer from the bottom slope is convected away by the flow. From (12), it is clear that the flow velocity increases with time. Initially, as the flow velocity is small, the heat conducted into the boundary layer is greater than that convected away, and the layer keeps growing. As time increases, the flow velocity increases, and thus convection increases until the heat conducted into the boundary layer is balanced by that convected away. At this time, the thermal boundary layer stops growing and the flow becomes steady. If at this time the bottom thermal boundary layer has not grown to the full local water depth, then the thermal boundary layer is considered locally distinct.

The balance between conduction and convection in the energy equation can be expressed as:

$$\frac{uT_b}{x} \sim \frac{kT_b}{\delta_T^2}. \tag{14}$$

Again, the horizontal distance x measured from the tip is taken as the horizontal length scale here. The balance in (14) yields the time scale for the steady state of the thermal boundary layer:

$$t_c \sim x^{2/3} e^{A\eta x/3} Ra^{-1/3} \frac{h^{4/3}}{k}. \tag{15}$$

It is clear in (15) that the steady-state time increases with x. This is in agreement with the finding of Farrow & Patterson (1993*b*), although no quantitative description of the steady-state time was given in their investigation. The steady-state time scale t_c is now compared with $(k\eta^2)^{-1}$, which is the time scale for the switch of the dominant heating mode from bottom heat flux to direct absorption of radiation, as described earlier. The comparison yields that, if $Ra > \eta^6 h^4 e^{A\eta x} x^2$, which applies to most field situations in the near-shore regions, the bottom heating dominates over the direct absorption heating. If the thermal boundary layer is distinct at time t_c, it will remain so at the steady state. Substituting the steady-state time scale t_c into (8), (9) and (12), the steady-state scales for the thickness of the thermal boundary layer, the temperature and the velocity can be derived, respectively, as:

$$T_b \sim x^{1/3} e^{-5A\eta x/6} Ra^{-1/6} \frac{H_0}{k} h^{2/3}, \tag{16}$$

$$\delta_T \sim x^{1/3} e^{A\eta x/6} Ra^{-1/6} h^{2/3}, \tag{17}$$

$$u \sim x^{1/3} e^{-A\eta x/3} Ra^{1/3} k h^{-4/3}, \tag{18}$$

and the volumetric flow rate across a sectional plane at steady state is given by:

$$Q \sim u\delta_T \sim x^{2/3} e^{-A\eta x/6} k h^{-2/3} Ra^{1/6}. \tag{19}$$

It is clear from (18) that the steady-state velocity increases with x in the near-shore region where $x < (A\eta)^{-1}$, and decreases with x in the offshore region where $x > (A\eta)^{-1}$. Similarly the steady-state temperature in the thermal boundary layer increases in the region where $x < 0.4(A\eta)^{-1}$. Furthermore, the thickness of the thermal boundary layer increases monotonically with the horizontal position x.

Apart from revealing the dependency of thermal flow properties on the horizontal position x, the above scaling will enable the identification of regions with distinct flow features, such as local distinctness and local stability of the thermal boundary layer.

The condition for the presence of a distinct thermal boundary layer can be derived in two equivalent ways: $\delta_T < Ax$, i.e. the thickness of the thermal boundary at the steady state is less than the local water depth, or $t_c < t_d$, where t_d is the time for the thermal boundary layer to reach the water surface

$$t_d \sim A^2 x^2 / k. \tag{20}$$

Both inequalities reach the same condition

$$Ra > A^{-6} (h/x)^4 e^{A\eta x}. \tag{21}$$

Since $A^{-6}(h/x)^4 e^{A\eta x}$ is a function of the horizontal position x, it is denoted by $f_1(x)$ as

$$f_1(x) \sim A^{-6} (h/x)^4 e^{A\eta x}. \tag{22}$$

It is worth noting that the steady-state scales of (16)–(19) are derived under the assumption of $t_c < t_d$, hence these scales apply to distinct thermal boundary layers for which $Ra > f_1(x)$. For the near-shore region with an indistinct thermal boundary layer, i.e. $Ra < f_1(x)$, the thermal boundary layer will grow to the top surface at the time t_d before convection becomes significant enough to balance conduction. Substituting (20) into (8), (9) and (12), the steady-state scales for the thickness of the thermal boundary layer, the temperature and the velocity for the near-shore region with an indistinct thermal boundary layer are obtained as:

$$\delta_T \sim Ax, \tag{23}$$

$$T_b \sim Ax H_0 \mathrm{e}^{-A\eta x}/k, \tag{24}$$

$$u \sim k(A/h)^4 x^3 \mathrm{e}^{-A\eta x} Ra. \tag{25}$$

The volumetric flow rate at steady state for an indistinct boundary layer in the near-shore region is given by:

$$Q \sim u\delta_T \sim kA^5(x/h)^4 \mathrm{e}^{-A\eta x} Ra. \tag{26}$$

3.3. *Thermal boundary-layer instability*

As noted earlier, the presence of an adverse temperature gradient in the bottom thermal boundary layer causes the thermal boundary layer to be potentially unstable. A Rayleigh–Bénard-type instability sets in if the adverse temperature gradient exceeds a critical value, or if $Ra_L > Ra_c$, where Ra_L is the local Rayleigh number of the thermal boundary layer, defined as

$$Ra_L \sim \frac{g\beta T_b \delta_T^3}{\nu k} \sim Ra\left(\frac{t}{h^2/k}\right)^2 \mathrm{e}^{-A\eta x}, \tag{27}$$

and Ra_c is the critical Rayleigh number of an inclined thermal layer which can be approximated by (Kurzweg 1970):

$$Ra_c = Ra_c(0^\circ)/\cos\theta, \tag{28}$$

where θ is the inclined angle of the thermal layer, and $Ra_c(0^\circ)$ is the critical Rayleigh number for horizontal fluid layers. $Ra_c(0^\circ) = 1101$ for a rigid free-boundary configuration with constant temperatures on the bounding surfaces and a linear temperature profile across the depth of the fluid layer (Drazin & Reid 1981). This value is used in (28) for later calculations following Lei & Patterson (2002). It will become clear that the exact value of Ra_c does not affect any subsequent discussions and conclusions (also refer to Lei & Patterson 2002).

It is clear from (27) that the local Rayleigh number increases with time. Instability sets in at a time t_B given by:

$$t_B \sim \left(\frac{Ra_c}{Ra}\right)^{1/2} \frac{h^2}{k} \mathrm{e}^{A\eta x/2}. \tag{29}$$

The above scale indicates that the time for the onset of instability increases with the horizontal position x. Although scale (27) suggests that Ra_L increases with time, there is an upper limit for the growth of Ra_L with time. When the flow reaches its steady state at t_c, both T_b and δ_T reach their maximum values, and thus the maximum Ra_L is given by $Ra_L(t_c)$. If $Ra_L(t_c) < Ra_c$, then the flow is always stable. In other words, instability, if present, has to occur before the steady-state time t_c. Therefore, the condition for the thermal flow to become unstable can be derived in two equivalent

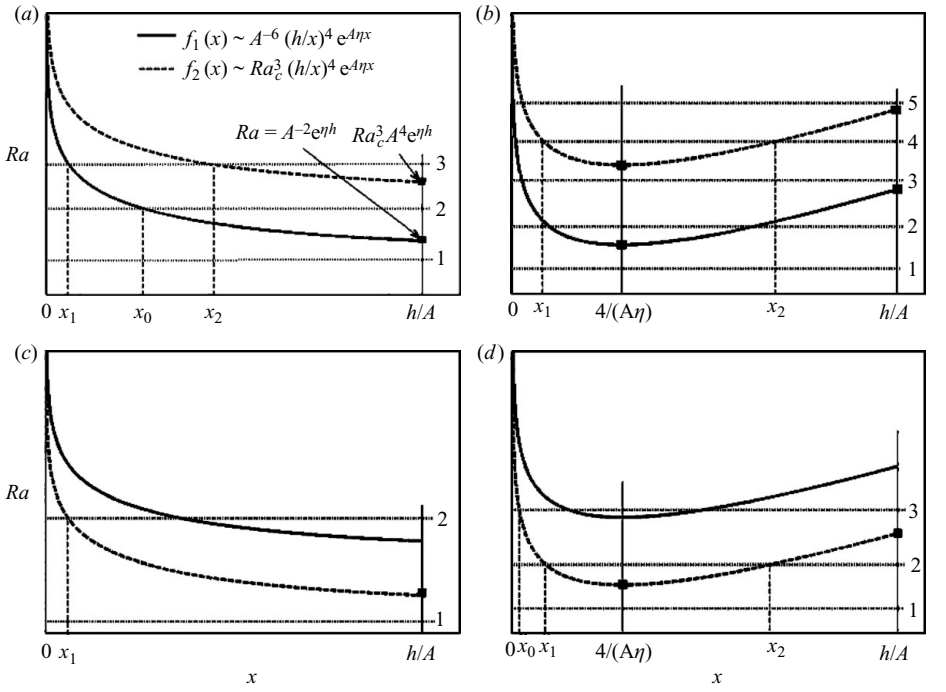

FIGURE 2. Typical profiles of $f_1(x)$ and $f_2(x)$ for (*a*) $A > Ra_c^{-1/2}, h < 4/\eta$; (*b*) $A > Ra_c^{-1/2}, h > 4/\eta$; (*c*) $A < Ra_c^{-1/2}, h < 4/\eta$; and (*d*) $A < Ra_c^{-1/2}, h > 4/\eta$; Horizontal dotted lines represent typical flow regimes. Rayleigh-number values of the filled squares separate the different Rayleigh-number regimes.

ways: (i) $Ra(t_c) > Ra_c$ or (ii) $t_c > t_B$. Both approaches give the same condition of

$$Ra > Ra_c^3 \left(\frac{h}{x}\right)^4 e^{A\eta x}. \tag{30}$$

Since $Ra_c^3(h/x)^4 e^{A\eta x}$ is a function of the horizontal position x, it is denoted by $f_2(x)$ as

$$f_2(x) \sim Ra_c^3 \left(\frac{h}{x}\right)^4 e^{A\eta x}. \tag{31}$$

4. Discussion of possible flow regimes

Two critical functions of the Rayleigh number, $f_1(x)$ and $f_2(x)$, have been derived for characterizing the thermal boundary-layer flow. Both functions represent thresholds for the presence of different flow regimes. If $Ra > f_1(x)$, the thermal boundary layer is distinct; and if $Ra > f_2(x)$, Rayleigh–Bénard instability sets in at time t_B.

The comparison between $f_1(x)$ and $f_2(x)$ yields that if $A > Ra_c^{-1/2}$, $f_1(x) < f_2(x)$ for all x; and if $A < Ra_c^{-1/2}$, $f_1(x) > f_2(x)$ for all x. Calculations of the derivative of $f_1(x)$ and $f_2(x)$ show that both $f_1(x)$ and $f_2(x)$ decrease with x for $x < 4/(A\eta)$, and increase with x for $x > 4/(A\eta)$. Because the range of x under consideration is $0 < x < h/A$, there are four possible scenarios, as shown in figure 2:

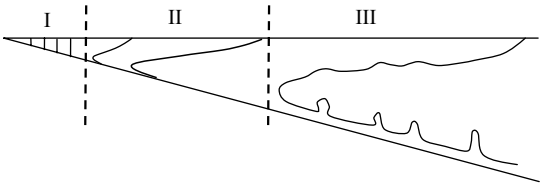

FIGURE 3. Sketches of expected isotherms for different flow subregions: (I) $Ra < f_1(x)$, indistinct, conductive; (II) $f_1(x) < Ra < f_2(x)$, distinct, stable convective; (III) $Ra > f_2(x)$, unstable convective.

(*a*) $A > Ra_c^{-1/2}$, $h < 4/\eta$: shallow waters with relatively large bottom slopes (figure 2*a*);

(*b*) $A > Ra_c^{-1/2}$, $h > 4/\eta$: deep waters with relatively large bottom slopes (figure 2*b*);

(*c*) $A < Ra_c^{-1/2}$, $h < 4/\eta$: shallow waters with relatively small bottom slopes (figure 2*c*);

(*d*) $A < Ra_c^{-1/2}$, $h > 4/\eta$: deep waters with relatively small bottom slopes (figure 2*d*).

Each of the horizontal lines in figure 2 represents a typical value of the Rayleigh number which results in different flow regimes in the respective scenarios. The following discussion of various flow regimes will focus mainly on scenario (*a*). Possible flow regimes are discussed briefly for the other three scenarios. Detailed discussion of the other scenarios can be made following the same procedures as outlined for scenario (*a*) below.

(*a*) $A > Ra_c^{-1/2}$, $h < 4/\eta$

In this case, $f_1(x) < f_2(x)$. Since $h < 4/\eta$ and $x < h/A$, then $x < 4/(A\eta)$. Both $f_1(x)$ and $f_2(x)$ decrease monotonically with x over the entire range of x and reach their respective minimum values at $x = h/A$, where

$$f_1(h/A) \sim A^{-2}\mathrm{e}^{\eta h}, \tag{32}$$

$$f_2(h/A) \sim Ra_c^3 A^4 \mathrm{e}^{\eta h}. \tag{33}$$

The analysis of Lei & Patterson (2002) is conducted under the assumption of $h < 1/\eta$ and hence is covered in this scenario. Under the specified condition, a full flow domain may consist of three subregions with distinct features illustrated by the sketched isotherms in figure 3. Region I is a conductive region; Region II is a stable convective region; and Region III is an unstable convective region. More detailed features of each of these subregions are described below, and will be demonstrated by the numerical simulations. For a given Rayleigh number, the actual flow domain may consist of one or two or all three subregions, depending on the comparisons between the Rayleigh number and the two critical Rayleigh numbers given in (32) and (33), as illustrated in figure 2(*a*) and described below.

(i)$Ra < A^{-2}\mathrm{e}^{\eta h}$ (line 1 in figure 2*a*). In this regime, Ra is smaller than both $f_1(x)$ and $f_2(x)$ over the entire domain. Therefore, according to the above-described criteria, the thermal boundary layer is indistinct and stable. In this case, the thermal boundary layer grows steadily and eventually encompasses the entire domain before convection becomes significant. Therefore, the heat transfer is dominated by conduction over the entire domain in this flow regime, corresponding to Region I in figure 3.

(ii)$A^{-2}\mathrm{e}^{\eta h} < Ra < Ra_c^3 A^4 \mathrm{e}^{\eta h}$ (line 2 in figure 2*a*). In this regime, $Ra < f_2(x)$ for all x, and thus the thermal boundary layer is stable over the entire domain. However, the thermal flow changes its property at a position x_0 where x_0 is determined from $f_1(x_0) \sim Ra$. For $x < x_0$, $Ra < f_1(x)$, the thermal boundary layer is indistinct at

the steady state with conduction dominating the heat transfer, corresponding to Region I in figure 3; for $x > x_0$, $Ra > f_1(x)$, the thermal boundary is distinct, and convection becomes significant in heat transfer, corresponding to Region II in figure 3. Therefore, the horizontal position x_0 marks the dividing position where the thermal boundary layer changes from indistinct to distinct and the dominant mode of heat transfer switches from conduction to convection. This theoretical prediction is easy to understand intuitively: since the water is shallow near the tip region, it takes less time for the thermal boundary layer to grow to the full local water depth. Therefore, the thermal boundary layer reaches the top surface before convection becomes significant. On the other hand, in the deeper region, it takes a longer time for the thermal boundary layer to grow to the full local water depth. Before that happens, convection becomes comparable with conduction, and thus the thermal boundary layer stops growing and remains distinct at the steady state.

(iii)$Ra > Ra_c^3 A^4 e^{\eta h}$ (line 3 in figure 2*a*). In this regime, a constant Ra line intersects both $f_1(x)$ and $f_2(x)$. The two crossing points, denoted by x_1 and x_2, respectively, in figure 2(*a*) ($f_1(x_1) \sim Ra$, $f_2(x_2) \sim Ra$), divide the entire flow domain into three subregions, corresponding to the three subregions sketched in figure 3. For $x < x_1$, Ra is smaller than both $f_1(x)$and $f_2(x)$, the thermal boundary layer is indistinct and stable, and heat transfer in this subregion is dominated by conduction. For $x_1 < x < x_2$, $f_1(x) < Ra < f_2(x)$, the thermal boundary layer is distinct and stable, and heat transfer in this subregion is dominated by stable convection. For $x > x_2$, $Ra > f_2(x)$, initially the thermal boundary layer grows by thermal diffusion; at time t_B scaled in (29), the instability sets in, and the thermal boundary layer becomes unstable before it reaches a steady state. Subsequently, both primary and secondary convections participate in this region, and the subregion is classified as an unstable convection region.

(*b*) $A > Ra_c^{-1/2}$ and $h > 4/\eta$

In this case, $f_1(x) < f_2(x)$ and the water is relatively deep. Both $f_1(x)$ and $f_2(x)$ reach their minimum values at $x = 4/(A\eta)$, and increase with x for $x > 4/(A\eta)$ (figure 2*b*). There are five possible flow regimes depending on Ra, as indicated by the five horizontal dashed lines in figure 2(*b*). It is worth noting that, in the flow regime of $f_2(4/(A\eta)) < Ra < f_2(h/A)$, i.e. $(e/4)^4 Ra_c^3 A^4 \eta^4 h^4 < Ra < Ra_c^3 A^4 e^{\eta h}$, as represented by the horizontal line 4, the thermal boundary layer is locally unstable only within a region of $x_1 < x < x_2$, where x_1 and x_2 are determined from $f_2(x) \sim Ra$, with stable regions on both the near shore and offshore sides of this region. The prediction of an unstable region centred away from the shore is consistent with the finding of Farrow & Patterson (1993*b*) based on a quasi-static linear stability analysis.

(*c*) $A < Ra_c^{-1/2}$ and $h < 4/\eta$

In this case, $f_1(x) > f_2(x)$ for all x and both $f_1(x)$ and $f_2(x)$ decrease with x over the entire region (figure 2*c*). The critical Rayleigh number for instability to occur is smaller than the critical Rayleigh number for the presence of a distinct boundary layer. For $Ra > f_2(h/A) \sim Ra_c^3 A^4 e^{\eta h}$, instability occurs in the region $x > x_1$ (refer to figure 2*c*) at time t_B before the thermal boundary layer becomes steady. Once the instability sets in, the growth of the thermal boundary layer is disturbed, and thus will no longer follow the scale (8). Therefore, the first critical function of the Rayleigh number $f_1(x)$ for the presence of a distinct thermal boundary layer, which is obtained based on the comparison of the steady-state boundary-layer thickness with the local water depth, is no longer relevant. As a consequence, there are only two possible flow regimes in this case, represented by the two horizontal dashed lines in figure 2(*c*).

(*d*) $A < Ra_c^{-1/2}$ and $h > 4/\eta$

In this case, $f_1(x) > f_2(x)$ for all x, and both $f_1(x)$ and $f_2(x)$ reach their minimum values at $x = 4/(A\eta)$ and increase with x for $x > 4/(A\eta)$ (figure 2*d*). Similar to the previous scenario, $f_1(x)$ is no longer relevant since instability disturbs the growth of the thermal boundary layer. Instability occurs if $Ra > f_2(4/(A\eta))$, i.e. $Ra > (\mathrm{e}/4)^4 Ra_c^3 A^4 \eta^4 h^4$. If $f_2(4/(A\eta)) < Ra < f_2(h/A)$, i.e. $(\mathrm{e}/4)^4 Ra_c^3 A^4 \eta^4 h^4 < Ra < Ra_c^3 A^4 \mathrm{e}^{\eta h}$, which is represented by line 2 in figure 2(*d*), instability occurs in the region of $x_1 < x < x_2$, where x_1 and x_2 are determined from $f_2(x) \sim Ra$. If $Ra > f_2(h/A)$, i.e. $Ra > Ra_c^3 A^4 \mathrm{e}^{\eta h}$, instability occurs in the region of $x > x_0$, where x_0 is also determined from $f_2(x) \sim Ra$.

In summary, the present analysis reveals a more complete and detailed flow panorama with four possible scenarios, depending on the bottom slope and the maximum water depth. For each scenario, the entire flow domain may be composed of several subregions with distinct flow and thermal features, depending on the Rayleigh number. In the following sections, numerical simulations are conducted to examine the possible flow regimes and distinct thermal flow features for scenario (*a*).

5. Numerical procedures

5.1. *Governing equations*

With radiation continuously entering from the surface and absorbed by the water body and the assumption of no energy loss through any boundary, the temperature of the water body keeps increasing. In this sense, there is no steady state with respect to the water temperature. However, a quasi-steady state will be reached in which the temperature gradient and flow velocity become steady. At the quasi-steady state, temperature increases at the same rate everywhere, and thus the difference between the local temperature and the average temperature becomes steady. The non-dimensional form of the new set of governing equations containing this temperature difference can be derived from (1)–(4) following the procedures outlined in Lei & Patterson (2002):

$$\frac{\partial u}{\partial x} + \frac{\partial v}{\partial y} = 0, \tag{34}$$

$$\frac{\partial u}{\partial t} + u\frac{\partial u}{\partial x} + v\frac{\partial u}{\partial y} = -Pr\ Ra\frac{\partial p}{\partial x} + Pr\nabla^2 u, \tag{35}$$

$$\frac{\partial v}{\partial t} + u\frac{\partial v}{\partial x} + v\frac{\partial v}{\partial y} = -Pr\ Ra\frac{\partial p}{\partial x} + Pr\nabla^2 v + Pr\ RaT, \tag{36}$$

$$\frac{\partial T}{\partial t} + u\frac{\partial T}{\partial x} + v\frac{\partial T}{\partial y} = \nabla^2 T + (\eta \mathrm{e}^{\eta y} - 2). \tag{37}$$

Here, all the quantities have been normalized with the following scales: the length scale x, y , $1/\eta \sim h$; the time scale; $t \sim h^2/k$; the temperature scale $T \sim H_0 h/k$; the velocity scale: u, $v \sim k/h$; and the pressure gradient scale: p_x, $p_y \sim \rho_0 g H_0 h/k$.

5.2. *Numerical method*

The governing equations (34)–(37) along with the specified boundary and initial conditions are solved numerically using a finite-volume method. The SIMPLE scheme is adopted for pressure–velocity coupling; and the QUICK scheme is applied for spatial derivatives. A second-order implicit scheme is applied for time discretization in calculating the transient flow.

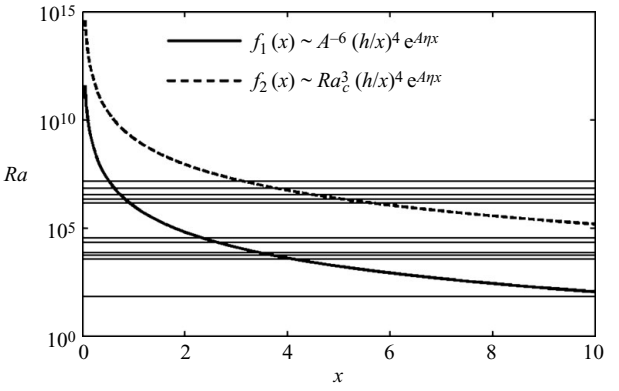

FIGURE 4. A typical profile of $f_1(x)$ and $f_2(x)$ for scenario (a) plotted with parameter values used in numerical simulations, horizontal lines represent Ra values used in the numerical simulations.

The simulation is conducted in a triangular domain of a dimensionless depth of $h = 1$ and a bottom slope of $A = 0.1$, with a non-dimensional attenuation coefficient $\eta = 0.12$ and a Prandtl number $Pr = 7$. This parametric setting is relevant to Scenario (a) discussed in § 4, which is re-plotted with the above non-dimensional values in figure 4. The horizontal lines in figure 4 represent the actual values of Ra used in the numerical simulations. It is clear that the selected Ra values cover all three possible flow regimes for this scenario. In order to avoid a singularity at the tip, the tip is cut off at $x = 0.2$, and an extra non-slip and adiabatic vertical wall is assumed there. Similar treatment of the tip region was carried out in Lei & Patterson (2002), and no significant modification to the flow was observed.

A mesh and time-step dependency test has been conducted for the case of $Ra = 1.4 \times 10^7$ (in the regime $Ra > Ra_c^3 A^4 e^{\eta h}$) using four different meshes, 211×71, 315×105, 421×141, 631×211. The flow domain is meshed with a non-uniform grid which has an increasing density towards all of the boundaries. The time steps for different meshes are adjusted accordingly so that the CFL (Courant–Friedrichs–Lewy) number remains the same for all meshes. The time histories of the maximum negative velocity within the bottom boundary layer at $x = 3.33$ are plotted in figure 5 for the coarsest and finest, meshes, respectively. Here, the same set of data is plotted using both linear (figure 5*a*) and logarithmic (figure 5*b*) time scales in order to show clearly the features at different stages of the flow development.

It is clear in figure 5 that three stages of the flow development can be identified in both solutions. At the initial stage, the solutions with the two meshes are virtually identical. At the transitional stage when instability starts to set in, the two solutions deviate from each other since instability is very sensitive to perturbations resulting from numerical errors, which depend strongly on the grid resolution. However, the patterns of strong fluctuations are present in both solutions at this stage. At the quasi-steady stage, the fluctuation of the maximum velocity becomes regular for both solutions with similar frequency and amplitude. The maximum negative velocities averaged from $t = 0.10$ to 0.25 for the four different meshes are (from coarsest to the finest): -230.8, -228.6, -227.6 and -227.1, indicating that as the mesh resolution increases, the predicted maximum velocity converges to a constant. The difference of the averaged maximum velocity between the meshes 421×141 and 631×211 is approximately 0.22 %. Furthermore, since the Rayleigh number tested here belongs

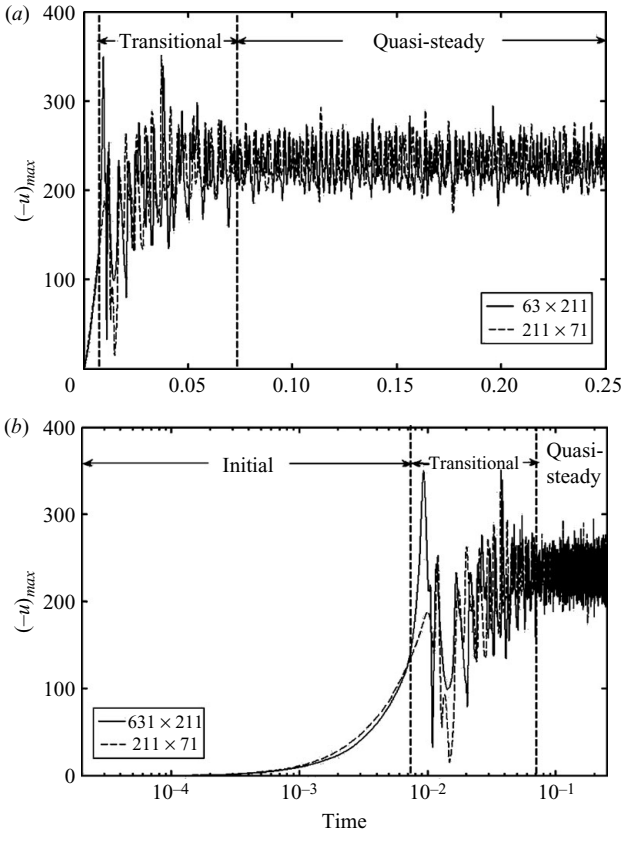

FIGURE 5. Time histories of the maximum negative horizontal component of velocity in the bottom boundary layer obtained along the vertical line at $x = 3.33$ for $Ra = 1.4 \times 10^7$ with two different meshes; (*a*) with a linear time scale (*b*) with a logarithmic time scale.

to the unstable flow regime and is the highest among all the calculated cases, the effect of the grid resolution on the solution is expected to be even less significant for other cases with lower *Ra*. In order to ensure the accuracy of the solutions while keeping the calculation time manageable, the grid 421×141 is used in all the following simulations. For the chosen mesh, the minimum face area is 0.0024; the maximum is 0.5125; and the maximum stretch factor is 1.07. The time step adopted for this mesh is 2.0×10^{-5}, giving a maximum CFL number of 1.02 for the present Rayleigh number.

6. Numerical verification of the scaling analysis

Since the above scaling analysis has unveiled detailed features of the flow in the triangular enclosure that are not revealed in Lei & Patterson (2002), in particular the variation of the flow features with x and the existence of distinct sub flow regions at sufficiently high *Ra*, the focus of this section will be on the validation of these newly revealed flow features.

To characterize the thermal features at different horizontal positions, the horizontal heat transfer rates by conduction and convection, averaged over the local water depth, are calculated at different horizontal positions. The total horizontal heat transfer rate

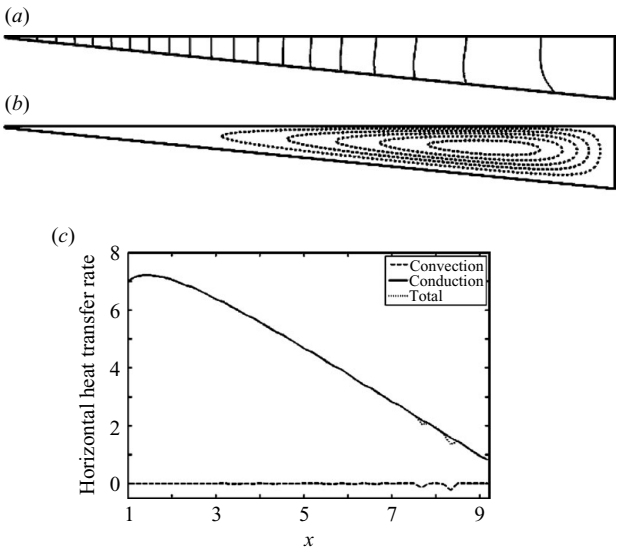

FIGURE 6. Features of the thermal flow at a low Ra ($Ra < A^{-2}e^{\eta h}$) at the steady state. (*a*) Isotherms with an interval of 2.11, (*b*) streamlines with an interval of 0.0525 of clockwise flow and (*c*) profile of the horizontal heat transfer rate averaged over the local water depth for $Ra = 70$.

with the combined effect of convection and conduction is defined in dimensionless form as:

$$H(x) = \frac{1}{Ax}\int_{-Ax}^{0}\left(uT_1 - \frac{\partial T_1}{\partial x}\right)\mathrm{d}y, \tag{38}$$

where $H(x)$ is normalized by I_0.

6.1. *Flow scenarios and distinctive regions in different regimes*

6.1.1. $Ra < A^{-2}e^{\eta h}$

With the current parametric setting, $A^{-2}e^{\eta h} \approx 112.75$, a simulation at $Ra = 70$ is conducted to demonstrate the flow and thermal features in this regime as represented by line 1 in figure 2(*a*). Figure 6 shows the isotherms, streamlines and horizontal heat transfer rates calculated at steady state. The nearly vertical isotherms in figure 6(*a*) suggest almost no temperature variation in the vertical direction, which is in agreement with the scaling expectation of an indistinct thermal boundary layer. Conduction associated with the horizontal temperature gradient dominates the heat transfer for the entire domain, as confirmed in figure 6(*c*). A clockwise flow is induced by the buoyancy force, as shown by the streamlines in figure 6(*b*).

6.1.2. $A^{-2}e^{\eta h} < Ra < Ra_c^3 A^4 e^{\eta h}$

In this medium-Rayleigh-number regime, two subdomains are predicted from the scaling analysis (refer to line 2 in figure 2*a*): a near-shore region with indistinct thermal boundary layer and an offshore region with distinct thermal boundary layer. It is expected that the flow remains stable over the entire domain. The isotherms and the horizontal heat transfer rates from numerical simulations are plotted in figure 7 for two typical Ra values ($Ra = 3500$ and 35 000) within this regime. It is clear that the characteristics of the isotherms vary with the horizontal position x: the nearly vertical isotherms in the near-shore region gradually transfer into curved

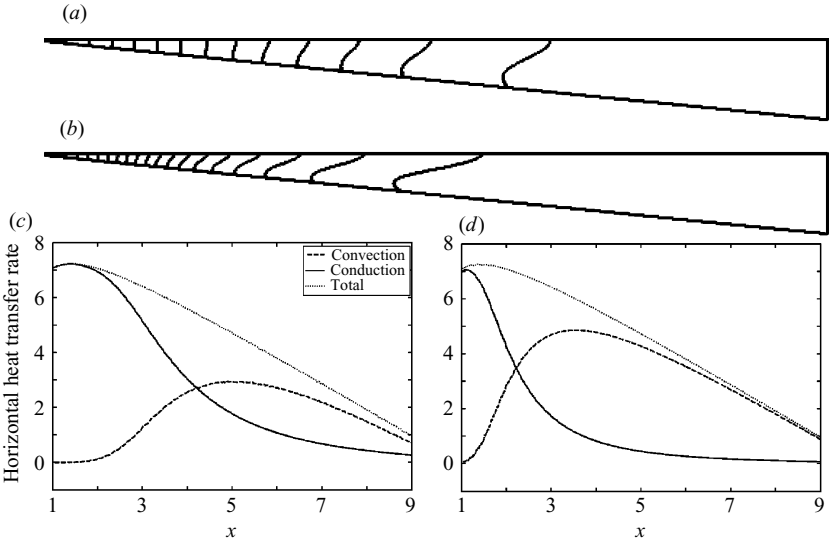

FIGURE 7. Features of thermal flow in the medium Ra regime ($A^{-2}e^{\eta h} < Ra < Ra_c^3 A^4 e^{\eta h}$) at the steady state. ($a$) Isotherms with an interval of 1.6887 for $Ra = 3500$, (b) isotherms with an interval of 0.8444 for $Ra = 35\,000$, and profiles of the horizontal heat transfer rate at (c) $Ra = 3500$ and (d) $Ra = 35\,000$.

isotherms with increasing curvature as x increases, suggesting that convection plays an increasingly important role in heat transfer in the offshore direction. The vertical isotherms confirm the feature of an indistinct thermal boundary layer, whereas the curved isotherms indicate the presence of a distinct thermal boundary layer. Compared with figure 7(a) for $Ra = 3500$, the curved isotherms in figure 7(b) for $Ra = 35\,000$ expand toward the shore as Ra increases, which is in qualitative agreement with the scaling prediction shown in figure 2(a).

To further ascertain the dividing positions quantitatively from the numerical data, the horizontal heat transfer rates averaged over the local depth are presented in figures 7(c) and 7(d) with respect to the horizontal position x. The position where convection transfer is equal to conduction transfer is considered as the dividing position between the two distinct subregions. Comparison between figures 7(c) and 7(d) suggests that the dividing position shifts toward the shore as Ra increases.

The dividing positions obtained from the numerical simulations as described above are plotted against that from the scaling analysis (by solving x_0 numerically from $f_1(x_0) \sim Ra$) in figure 8 for a range of Rayleigh numbers. It is noted that the results obtained for the high-Rayleigh-number regime $Ra > Ra_c^3 A^4 e^{\eta h}$ (see § 6.1.3) are also included in figure 8. The numerical data are grouped into two categories in figure 8, one termed 'Unstable', representing the data for $Ra > Ra_c^3 A^4 e^{\eta h}$; and the other termed 'Stable', representing the data for $A^{-2}e^{\eta h} < Ra < Ra_c^3 A^4 e^{\eta h}$ as discussed in this section. The boundary between these two sets of data is approximately indicated by the vertical dashed line in figure 8. It is seen in this figure that, as the Rayleigh number increases, the dividing position moves toward the shore, suggesting the shrinkage of the conduction-dominated regions. The clear linear correlation between the numerical data and scaling prediction shown in figure 8 suggests that the dividing position between the conduction-dominated region and the convection-dominated region is predicted well by the scaling analysis.

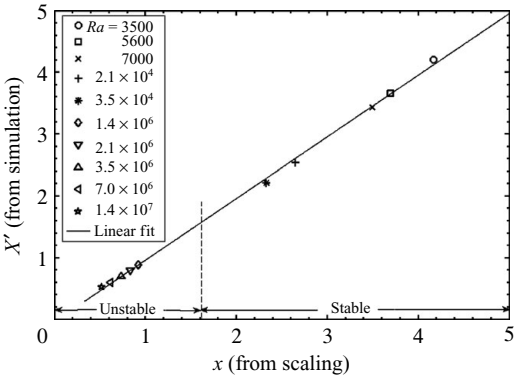

FIGURE 8. Dividing position between conduction-dominated and convection-dominated regions from the numerical simulation versus that from scaling analysis. The dashed line represents the predicted minimum value of the dividing position under a stable condition from scaling analysis.

6.1.3. $Ra > Ra_c^3 A^4 e^{\eta h}$

In this high-Rayleigh-number regime, three distinct subregions are predicted by scaling analysis (refer to line 3 in figure 2*a*): a near-shore conductive region ($x < x_1$); a middle stable convective region ($x_1 < x < x_2$); and an unstable convective offshore region ($x > x_2$). The thermal flow features in these three distinct regions are revealed in figure 9 with simulation results for two different Ra values ($Ra = 1.4 \times 10^6$ and 1.4×10^7).

The increasing temperature gradient towards the shore leads to an increasing density of isotherms toward the shore as shown in figures 9(*a*) and 9(*b*), where subregions with distinct features can be identified. The subregion with an indistinct thermal boundary layer characterized by the vertical isotherms occupies a relatively smaller area than in the cases in the medium range of Ra. The isotherms change from nearly vertical lines in the near-shore region into bent lines in the middle region and finally into wavy lines (representing uprising plumes) in the offshore region, confirming the scaling prediction of three distinct subregions. Furthermore, a comparison between figures 9(*a*) and 9(*b*) suggests that both the region with an indistinct thermal boundary layer and the region with a stable thermal boundary layer shrink, whereas the unstable region expands, as the Rayleigh number increases; this is consistent with the scaling prediction.

Streamlines at steady state obtained for $Ra = 1.4 \times 10^6$ and $Ra = 1.4 \times 10^7$ are shown in figures 9(*c*) and 9(*d*), respectively. Comparison suggests that the intensity, the wave number and the extent of instability all increase with Ra.

The horizontal heat transfer rates averaged over the local water depth are shown in figures 9(*e*) and 9(*f*). These plots provide a quantitative measurement of the dividing positions for different subregions. The position where conduction equals convection separates the conduction-dominated region from the convection-dominated region. The dependence of this dividing position on the Rayleigh number has been shown in figure 8. The position where convection starts to show wavy features divides the region dominated by stable convection from the region dominated by unstable convection.

To estimate the position where the instability starts to occur, time series of the horizontal convection at various horizontal positions are obtained, and standard deviations are calculated over a dimensionless time period of 0.04 during the quasi-steady state. In a stable steady flow, the standard deviation is zero; when instability

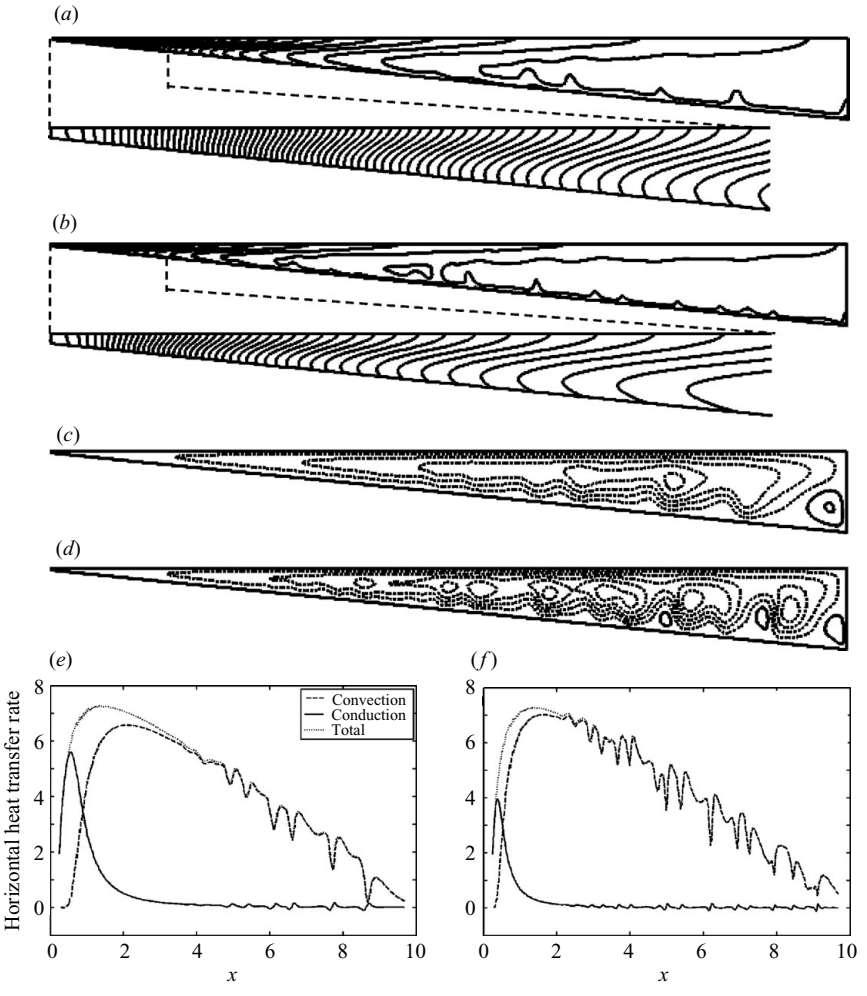

FIGURE 9. Features of thermal flow in the high Ra regime ($Ra > Ra_c^3 A^4 e^{\eta h}$) at the quasi-steady state. (a) Isotherms with an interval of 0.063 at $Ra = 1.4 \times 10^6$, (b) isotherms with an interval of 0.042 at $Ra = 1.4 \times 10^7$. The lower plots in (a) and (b) are enlarged views of the sections indicated by the dashed lines. (c) Streamlines with an interval of 7 at $Ra = 1.4 \times 10^6$. (d) Streamlines with an interval of 14 at $Ra = 1.4 \times 10^7$. Dashed streamlines represent clockwise flow, and solid streamlines represent anticlockwise flow. (e) and (f) are the profiles of the horizontal heat transfer rates averaged over local water depth for $Ra = 1.4 \times 10^6$ and $Ra = 1.4 \times 10^7$, respectively.

occurs, the standard deviation will increase. The calculated standard deviation is then plotted against the horizontal position x in figure 10(a) for a range of Rayleigh numbers. It is clear in figure 10(a) that the position where the standard deviation starts to increase moves toward the shore as the Rayleigh number increases. The positions where the standard deviation first exceeds a certain threshold (0.001) were obtained for different Rayleigh numbers. These positions approximately represent the boundary between the stable and unstable subregions, and are plotted against the scaling predictions (by solving x_2 numerically from $f_2(x_2) \sim Ra$) in figure 10(b). It is clear from figure 10(b) that the unstable region expands toward the shore as Ra increases. The good linear correlation shown in figure 10(b) confirms the scaling

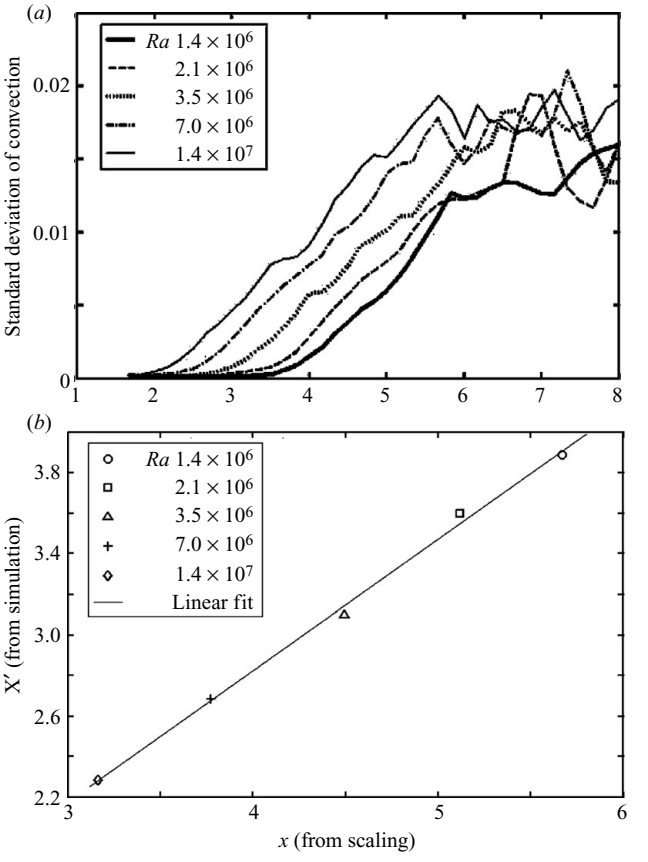

FIGURE 10. (*a*) Standard deviation of convection time series over a time period of 0.04 at the quasi-steady state. (*b*) Dividing position between the stable and unstable regions from numerical simulations versus the prediction from scaling.

prediction with regard to the dividing position between the stable and unstable regions.

The time series of the calculated horizontal heat transfer rate averaged over the local water depth for $Ra = 1.4 \times 10^6$ are shown in figure 11 for three representative horizontal positions, each dominated by a distinct heat transfer mode at quasi-steady state: conduction; stable convection; and unstable convection. In the region dominated by conduction (figure 11*a*), conduction dominates the horizontal heat transfer over the entire time series. In the region dominated by stable convection (figure 11*b*), convection gradually surpasses conduction and becomes the dominant mode of the horizontal heat transfer as time goes on. In the region dominated by unstable convection (figure 11*c*), instability sets in after a certain time, and both conduction and convection become unstable with unstable convection dominating the horizontal heat transfer. At the quasi-steady state, a spectral analysis of the time series indicates that the frequencies of the fluctuations of both conduction and convection remain approximately constant.

6.2. *Initial stage scaling*

At the initial stage, the exponentially decaying absorption of radiation with the water depth results in the dependency of the water temperature on the horizontal position x.

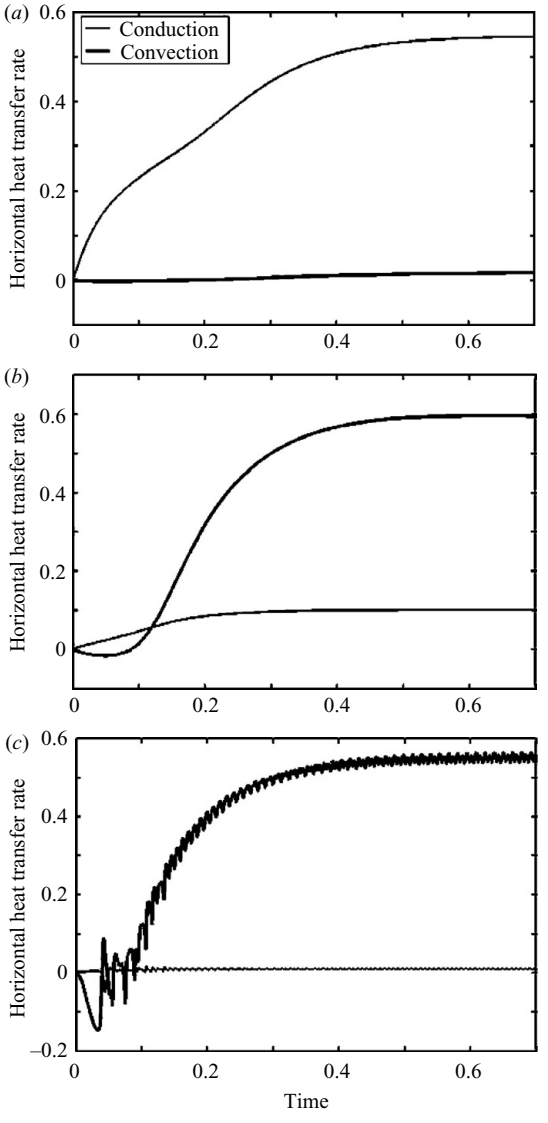

FIGURE 11. Time series of the horizontal heat transfer rates averaged over the local water depth at $Ra = 1.4 \times 10^6$ for three representative x positions (a) $x = 0.5$, (b) $x = 1.5$, (c) $x = 4$.

Here, both the time dependency and the x dependency of the initial temperature scale (9) are validated against numerical data in figures 12 and 13.

To validate the dependency of the temperature on time, the x position is fixed at $x = 5$ and the temperature profiles are extracted along the line normal to the bottom surface at different times (figure 12a). It is clear that T decreases away from the bottom boundary and becomes constant after a short distance, indicating the thermal boundary layer is only confined to a thin layer near the bottom surface at the initial stage. The position where T starts to become constant marks the outer edge of the thermal boundary layer, and thus it is clear from figure 12(a) that the thickness of the thermal boundary layer grows with time. After normalizing the distance and temperature by (8) and (9), respectively, the temperature profiles along the vertical

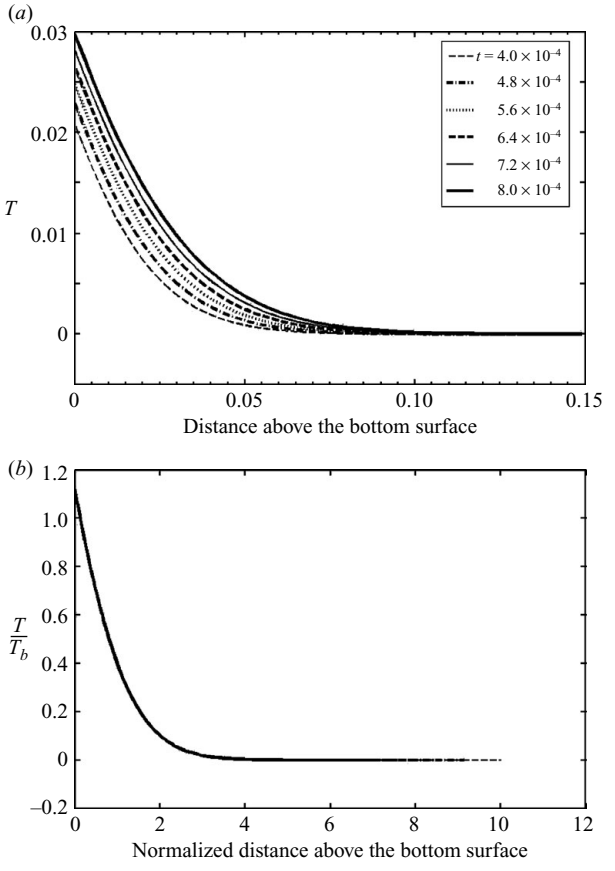

FIGURE 12. Verification of initial temperature scaling with respect to time at $x = 5.0$ (*a*) Temperature profiles normal to the bottom surface at different times. (*b*) Normalized temperature profiles.

line at different times collapse onto a single line (figure 12*b*), and thus the time dependency of δ_T and T_b specified in (8) and (9) is verified.

To validate the x dependency of T_b, temperature profiles along lines normal to the bottom surface at different x and at a fixed time $t = 8.0 \times 10^{-4}$ are shown in figure 13(*a*), and the normalized temperature profiles using the scales (8) and (9) are plotted in figure 13(*b*). The collapse of the temperature profiles at different x onto a single line in figure 13(*b*) clearly verifies the x dependency of the temperature, as specified in (9).

6.3. *Steady-state scaling for distinct regions*

Selected properties at the steady state are verified in this section. Since the present scaling analysis reveals the dependency of flow properties on the horizontal position x, emphasis will be placed on this x dependency in the following validation.

Two different sets of scaling for the steady-state boundary layer have been derived in § 3.2: scales (20) and (23)–(26) apply to an indistinct thermal boundary layer near shore which is dominated by conduction; scales (15)–(19) apply to a distinct thermal boundary layer dominated by stable convection. Through mass conservation, it can be derived that the velocity scale for the thermal boundary layer applies to the upper

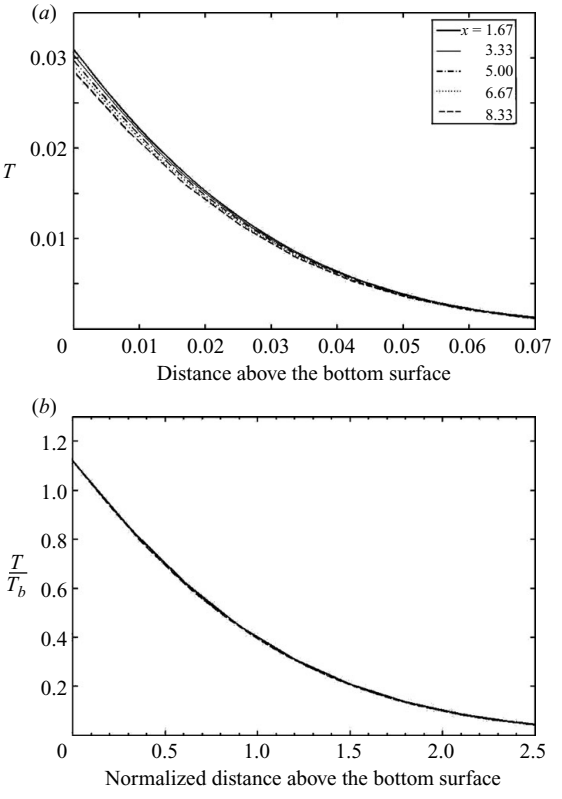

FIGURE 13. Verification of initial temperature scaling with respect to the horizontal position x at time $t = 8.0 \times 10^{-4}$. (*a*) Non-dimensional temperature profiles normal to the bottom surface at different non-dimensional x. (*b*) Normalized temperature profiles at different horizontal positions.

intrusion layer as well (Lei & Patterson 2002). The scales of the flow velocity and the volumetric flow rate of both sets of scaling are considered here. The volumetric flow rate characterizes the strength of the circulation, and is calculated numerically as:

$$Q(x) = 1/2 \int_{-Ax}^{0} |u| \, \mathrm{d}y. \tag{39}$$

6.3.1. *Conduction-dominated region*

For the conduction-dominated region, the flow velocity in the boundary layer is governed by (25). The calculated maximum velocities in both the boundary and intrusion layers at a number of horizontal locations within the conduction-dominated region are plotted against the dimensionless velocity scale in figure 14. It is clear that the maximum velocities in both the bottom and upper layers are represented well by the velocity scale (25). In particular, the dependency of the velocity on the horizontal position x revealed by the present scaling is verified. Another feature revealed in figure 14 is that the slope of the linear fit line is larger for the upper layer than that for the bottom layer (1.45 for the upper layer and 0.98 for the bottom layer), indicating stronger flow in the upper layer. This is a consequence of different boundary conditions (stress-free at the surface and non-slip at the bottom).

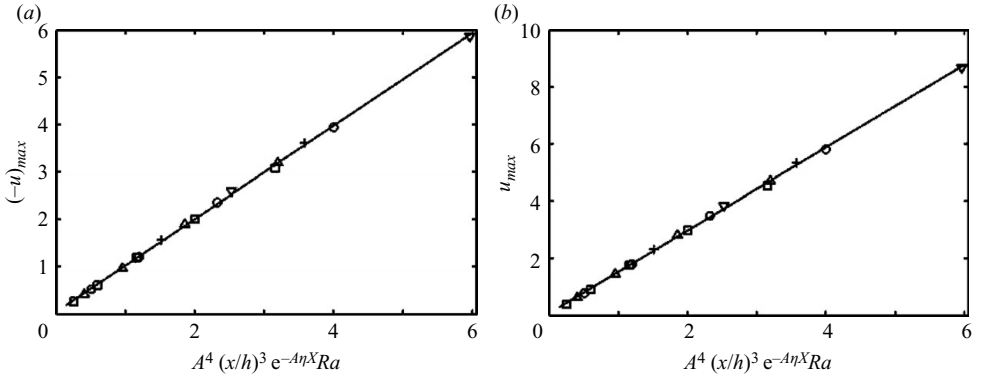

FIGURE 14. Maximum velocity extracted along vertical lines at different x positions within the conduction dominated region. (*a*) Maximum negative horizontal component of velocity in the bottom layer. (*b*) Maximum horizontal component of velocity in the upper layer. The x positions are extracted at equal intervals within the specified range. □, $Ra = 3500$ ($x = 0.9 \sim 2.1$); △, 5600 ($0.9 \sim 1.8$); ○, 7000 ($0.9 \sim 1.8$); +, 21 000 ($0.9 \sim 1.2$); ▽, 35 000 ($0.9 \sim 1.2$); —, linear fit.

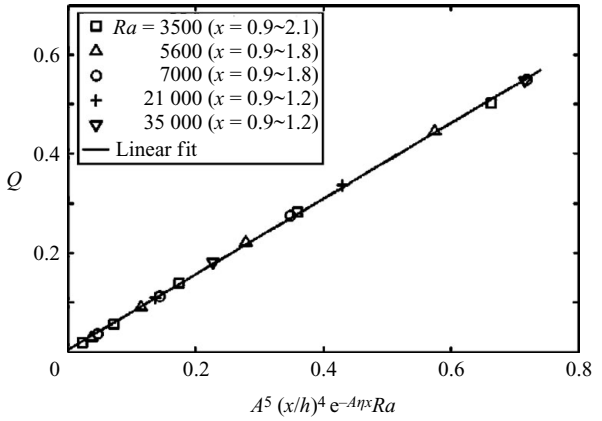

FIGURE 15. Volumetric flow rate at different x positions within the conduction-dominated near-shore region for different Rayleigh numbers. The x positions are equally spaced within the specified range.

The calculated volumetric flow rates within the conduction-dominated region are plotted against the non-dimensional form of scale (26) in figure 15. It is clear that the volumetric flow rate is represented well by the scaling.

6.3.2. *Regions dominated by stable convection*

For the convection-dominated region with a distinct and stable thermal boundary layer, the velocity scale (18) applies at the steady state. From (18), for shallow waters where $x < (A\eta)^{-1}$, the velocity increases with the horizontal position x. The calculated maximum velocities along vertical lines at different x positions within the stable convection region are plotted against the dimensionless form of (18) for both the bottom boundary layer and the upper layer in figure 16. The numerical results shown in figures 16(*a*) and 16(*b*) are obtained for a wide range of Rayleigh numbers, spanning both the stable and unstable flow scenarios. For clarity, only data at one x position are shown for each Ra within the stable regime in figures 16(*a*) and 16(*b*). The dependency of the velocity on x within the stable regime is further illustrated in

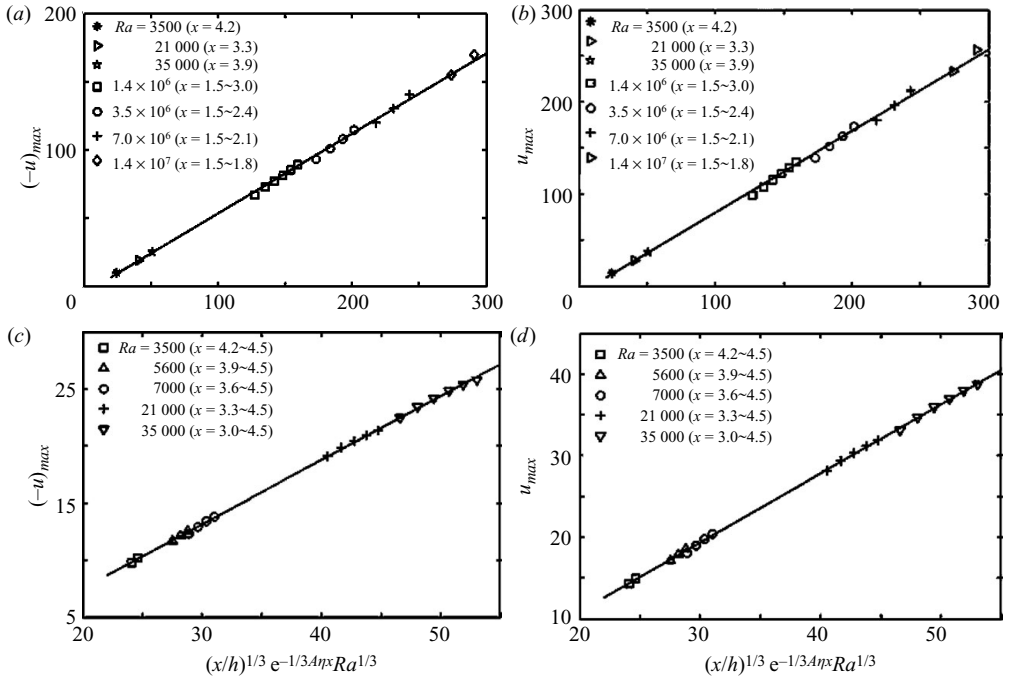

FIGURE 16. Maximum velocity extracted along vertical lines at various x positions within the stable convection region. The x positions are equally spaced within the specified range. (*a*) and (*c*) are maximum negative horizontal component of velocity in the bottom boundary layer. (*b*) and (*d*) are maximum horizontal component of velocity in the upper layer. —, linear fit.

figures 16(*c*) and 16(*d*). As noted before, the selected positions are located sufficiently far from the endwall to avoid the endwall effect.

Figure 16 demonstrates that (18) is an appropriate velocity scale for the region dominated by stable convection in both the medium Ra regime of $A^{-2}e^{\eta h} < Ra < Ra_c^3 A^4 e^{\eta h}$ and the high Ra regime of $Ra > Ra_c^3 A^4 e^{\eta h}$.

The numerically calculated volumetric flow rates in the medium Ra regime are plotted against the scaling prediction (19) in figure 17. The linear correlation clearly confirms that the volumetric flow rate is represented well by the scaling results.

6.4. *Critical time for the onset of instability*

The scaling result (29) given in § 3.3 suggests that the critical time for the onset of instability increases with the horizontal position x. The dependency of the critical time t_B on Ra specified in (29) has been verified in Lei & Patterson (2002). Therefore, the verification here is only concerned with the x dependency of the critical time t_B.

The critical time for the onset of instability has been determined through a direct stability analysis based on a three-dimensional model in Lei & Patterson (2003). In their numerical model, both random and single-mode perturbations are introduced over the sloping bottom, and the standard deviations of the temperature along the transverse direction at different x positions are recorded as time series. In principle, the critical time for the onset of instability corresponds to the time when the standard deviation starts to increase from an initially constant value. With the single-mode perturbation in place, the plot of the critical time for the onset of instability against the horizontal position x in Lei & Patterson (2003) shows that, apart from the tip region

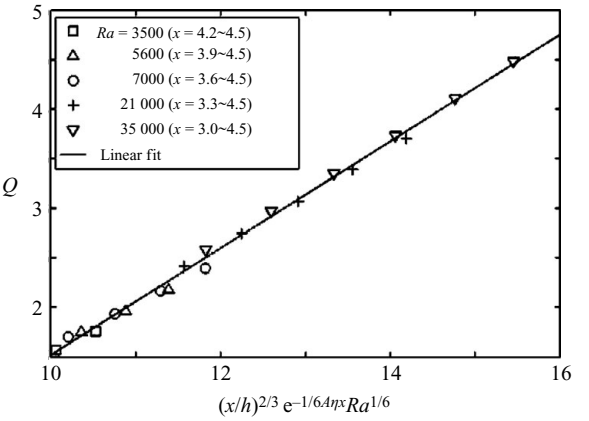

FIGURE 17. Volumetric flow rate at different x positions within the stable convection region under different Rayleigh numbers. The x positions are equally spaced within the specified range.

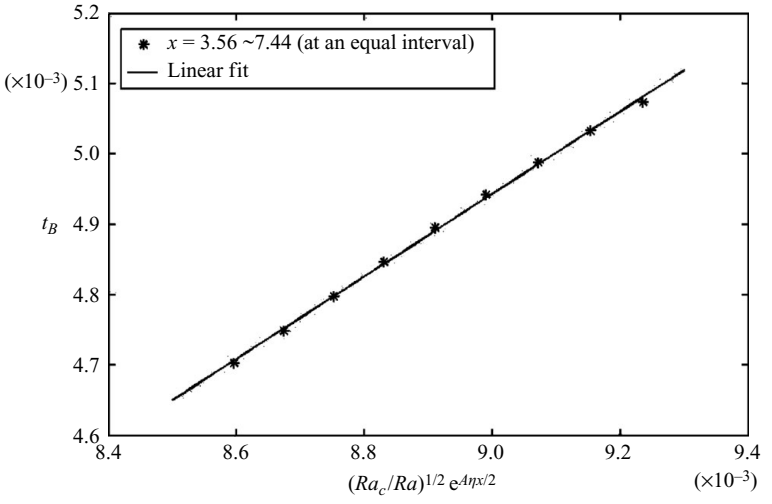

FIGURE 18. Critical time of instability at different horizontal positions from the numerical simulation of Lei & Patterson (2003) versus the present scaling prediction.

and the deep end region which are affected by the endwall, the critical time increases monotonically with the horizontal position x, which is in qualitative agreement with the present scaling analysis.

The critical time t_B obtained at different x positions from the direct stability analysis of Lei & Patterson (2003) is plotted against the present scaling prediction in figure 18. In order to avoid the effect of the two endwalls, the x positions are chosen between 3.56 and 7.44 at equal intervals. Here, the critical Rayleigh number Ra_c in (29) is calculated from (28). Although the exact value of Ra_c relevant to the present flow configuration remains unresolved, according to (29), it will only slightly affect the slope of the linear fitting line in figure 18 and will not change the linear correlation between the numerical data and the scaling prediction as long as Ra_c is a constant. Figure 18 suggests that the x dependency of the critical time predicted by the present scaling analysis is verified well by the reported results of the direct stability analysis.

Meanwhile, the present scaling presents a theoretical explanation for the increase of the critical time with the offshore distance x observed by Lei & Patterson (2003).

7. Conclusions

By recognizing the dependence of various flow quantities on the horizontal position with a variable length scale x and retaining the exponential term $e^{-A\eta x}$ arising from the non-uniform heat flux at the sloping bottom in the analysis, the present scaling reveals detailed features of natural convection induced by absorption of radiation in a triangular domain which are not shown in the previous scaling: the entire flow domain is separated into different subregions with distinct flow and thermal features. Furthermore, the present scaling also quantifies the variation of the flow properties with the horizontal position x in different regions. These newly predicted features are verified by numerical simulations.

Two critical functions for the Rayleigh number have been derived to characterize the flow features: $f_1(x) \sim A^{-6}(h/x)^4 e^{A\eta x}$ and $f_2(x) \sim Ra_c^3(h/x)^4 e^{A\eta x}$. The thermal boundary layer is distinct if $Ra > f_1(x)$ and unstable if $Ra > f_2(x)$. There are four possible flow scenarios depending on the bottom slope A and the maximum water depth h.

The flow scenario with $A > Ra_c^{-1/2}$ and $h < 4/\eta$ can be further classified into three different flow regimes according to the Rayleigh number, which are examined in detail in this study. The major features in each of the flow regimes are summarized below with respect to the dominant mode of horizontal heat transfer at steady state:

(i) $Ra < A^{-2}e^{\eta h}$. The entire domain is dominated by stable conduction.

(ii) $A^{-2}e^{\eta h} < Ra < Ra_c^3 A^4 e^{\eta h}$. The domain is composed of two distinct subregions (separated at offshore distance x_0 where $f_1(x_0) \sim Ra$): a near-shore region dominated by conduction and an offshore region dominated by stable convection.

(iii) $Ra > Ra_c^3 A^4 e^{\eta h}$. The domain consists of three distinct subregions (separated at offshore distance x_1 and x_2 where $f_1(x_1) \sim Ra$, $f_2(x_2) \sim Ra$): a near-shore region dominated by conduction, a central region dominated by stable convection, and an offshore region dominated by unstable convection.

Apart from identifying distinctive regions within the triangular flow domain, the present scaling also reveals the variation of flow and thermal features with the horizontal position x within distinct flow regions. Two sets of steady-state scales are derived for the conduction-dominated region (scale (20) and (23)–(26)) and the region dominated by stable convection (scale (15)–(19)), both embodying the horizontal position dependence. A time scale for the onset of instability in the unstable flow regime, which also depends on the horizontal position, is given in (29).

In a real-life situation, the intensity of solar radiation usually places the flow in regime (iii) above. Hence, instability induced by the absorption of radiation is present in a region offshore, the extent of which can be estimated from the present scaling analysis. Furthermore, the present scaling results are readily applicable to designing laboratory or geophysical experiments, since they provide detailed estimation of the magnitude of the temperature, the velocity, the steady-state time, and the time for the onset of instability at different horizontal positions, as well as the features and scopes of distinctive subregions for various flow scenarios.

In application of the scaling to field situations, many other geophysical factors must be accounted for, such as the unsteadiness of the flow due to the diurnal variation of the thermal forcing suggested by field experiments (Adams & Wells 1984; Monismith *et al.* 1990) and asymptotic solutions (Farrow 2004), the effect of the rotation of the

earth at large scales, the complex three-dimensional topography for which the two-dimensional model is not appropriate, and the interaction of the thermal flow with currents driven by other mechanisms (e.g. tides, wind-driven currents, waves, etc). In addition, the present scaling of velocity as a function of the offshore distance applies only to the regions dominated by conduction or stable convection. For unstable regions, the magnitude of the flow is significantly modulated by flow instabilities in the form of thermal plumes. Despite the simplification of the present model, the different flow scenarios and the variation of radiation-induced thermal flow with the offshore distance revealed by the present improved scaling analysis have significant implications for a comprehensive near-shore model.

The improved scaling analysis presented in this paper is concerned with constant thermal forcing induced by absorption of radiation. A similar scaling analysis can be carried out for boundary-layer flow in the wedge domain subject to constant heat loss from the water surface. The advancement in scaling for the constant thermal forcing in the wedge domain will also benefit a more realistic thermal forcing model of the diurnal heating and cooling cycle. Furthermore, the adoption of a varying length scale embodied in the present scaling can be applied to a wider range of similar problems.

The authors gratefully acknowledge the financial support of the Australian Research Council. Yadan Mao is grateful for the PhD scholarship jointly sponsored by the China Scholarship Council and James Cook University.

REFERENCES

Adams, E. E. & Wells, S. A. 1984 Field measurements on side arms of lake. *J. Hydraul. Engng.* ASLE**110**, 773–793.

Bejan, A., Al-Homoud, A. A. & Imberger, J. 1981 Experimental study of high-Rayleigh-number natural convection in a horizontal cavity with different end temperatures. *J. Fluid Mech.* **109**, 283–299.

Bejan, A. & Rossie, A. N. 1981 Natural convection in a horizontal duct connecting two fluid reservoirs. *J. Fluid Mech.* **109**, 283–299.

Coates, M. J. & Patterson, J. C. 1993 Unsteady natural convection in a cavity with non-uniform absorption of radiation. *J. Fluid Mech.* **256**, 133–161.

Coates, M. J. & Patterson, J. C. 1994 Numerical simulations of the natural convection in a cavity with nonuniform internal sources. *Intl J. Heat Fluid Flow* **15**, 218–225.

Cormack, D. E., Leal, L. G. & Imberger, J. 1974*a* Natural convection in a shallow cavity with differentially heated endwalls. Part 1. Asymptotic theory. *J. Fluid Mech.* **65**, 209–229.

Cormack, D. E., Leal, L. G. & Seinfeld, J. H. 1974*b* Natural convection in a shallow cavity with differentially heated endwalls. Part 2. Numerical solutions. *J. Fluid Mech.* **65**, 231–246.

Drazin, P. G. & Reid, W. H. 1981 *Hydrodynamic Stability*. Cambridge University Press.

Farrow, D. E. 2004 Periodically forced natural convection over slowly varying topography. *J. Fluid Mech.* **508**, 1–21.

Farrow, D. E. & Patterson, J. C. 1993*a* On the response of a reservoir sidearm to diurnal heating and cooling. *J. Fluid Mech.* **246**, 143–161.

Farrow, D. E. & Patterson, J. C. 1993*b* On the stability of the near shore waters of a lake when subject to solar heating. *Intl J. Heat Mass Transfer* **36**, 89–100.

Farrow, D. E. & Patterson, J. C. 1994 The daytime circulation and temperature structure in a reservoir sidearm. *Intl J. Heat Mass Transfer* **37**, 1957–1968.

Hart, J. E. 1972 Stability of thin non-rotating Hadley circulations. *J. Atmos. Sci.* **29**, 687–697.

Imberger, J. 1974 Natural convection in a shallow cavity with differentially heated endwalls. Part 3. Experimental results. *J. Fluid Mech.* **65**, 247–260.

Kurzweg, U. H. 1970 Stability of natural convection within an inclined channel. *Trans. ASME C: J. Heat Transfer* **92**, 190–191.

Lei, C. & Patterson, J. C. 2002 Unsteady natural convection in a triangular enclosure induced by absorption of radiation. *J. Fluid Mech.* **460**, 181–209.

Lei, C. & Patterson, J. C. 2003 A direct stability analysis of a radiation-induced natural convection boundary layer in a shallow wedge. *J. Fluid Mech.* **480**, 161–184.

Lei, C. & Patterson, J. C. 2005 Unsteady natural convection in a triangular enclosure induced by surface cooling. *Intl J. Heat Fluid Flow* **26**, 307–321.

Mao, Y., Lei, C. & Patterson, J. C. 2007 Natural convection in a triangular enclosure induced by solar radiation. *Proc. 16th Australasia Fluid Mechanics Conf. Gold Coast, Australia, 3–7 December 2007*, pp. 406–410.

Monismith, S. G., Imberger, J. & Morison, M. L. 1990 Convective motions in the sidearm of a small reservoir. *Limnol. Oceanogr.* **35**, 1676–1702.

Monismith, S. G., Genin, A. Reidenbach, M. A., Yahel, G., & Koseff, J. R. 2006 Thermally driven exchanges between a coral reef and the adjoining ocean. *J. Phys. Oceanogr.* **36**, 1332–1347.

Ostrach, S. 1988 Natural convection in enclosures. *Trans. ASME* C: *J. Heat Transfer* **110**, 1175–1190.

Patterson, J. C. 1984 Unsteady natural convection in a cavity with internal heating and cooling, *J. Fluid Mech.* **140**, 135–151.

Patterson, J. C. & Imberger, J. 1980 Unsteady natural convection in a rectangular cavity. *J. Fluid Mech.* **100**, 65–86.

Rabl, A. & Nielsen, C. E. 1975 Solar ponds for space heating. *Solar Energy* **17**, 1–12.

Trevisan, O. V. & Bejan, A. 1986 Convection driven by the nonuniform absorption of thermal radiation at the free surface of stagnant pool. *Numer. Heat Transfer* **10**, 483–506.